NJC

Accepted Manuscript

This is an *Accepted Manuscript*, which has been through the Royal Society of Chemistry peer review process and has been accepted for publication.

Accepted Manuscripts are published online shortly after acceptance, before technical editing, formatting and proof reading. Using this free service, authors can make their results available to the community, in citable form, before we publish the edited article. We will replace this *Accepted Manuscript* with the edited and formatted *Advance Article* as soon as it is available.

You can find more information about *Accepted Manuscripts* in the Information for Authors.

Please note that technical editing may introduce minor changes to the text and/or graphics, which may alter content. The journal's standard Terms & Conditions and the Ethical guidelines still apply. In no event shall the Royal Society of Chemistry be held responsible for any errors or omissions in this *Accepted Manuscript* or any consequences arising from the use of any information it contains.

ROYAL SOCIETY OF CHEMISTRY

www.rsc.org/njc

Hierarchical Growth of $ZnFe_2O_4$ for Sensing Applications

Ramkrishna Sahoo[†], Sumita Santra[‡], Chaiti Ray[†], Anjali Pal[§], Yuichi Negishi[‖], Samit Kumar Ray[‡] and Tarasankar Pal*[,†]

[†]Department of Chemistry, and [§]Department of Civil Engineering, Indian Institute of Technology, Kharagpur-721302, India

[‖]Department of Applied Chemistry, Tokyo University of Science, Tokyo-1628601, Japan

[‡] Department of Physics, Indian Institute of Technology, Kharagpur-721302, India

E-mail: *tpal@chem.iitkgp.ernet.in*

ABSTRACT:

Mesoporous $ZnFe_2O_4$ nanoflowers (NFs) have been prepared from modified hydrothermal (MHT) technique, developed in our laboratory. Urea has been brought in for hydrolysis of $FeCl_3$ and $ZnSO_4$ in solution to homogeneously precipitate $ZnFe_2O_4$. The precipitated product upon annealing at 450 °C results in mesoporous $ZnFe_2O_4$ NFs. Important physical methods have been used to characterize the NF material in the solid state. The growth mechanism of mesoporous NF of evolution is confirmed from the adopted reaction strategy. The $ZnFe_2O_4$ NF finds application in peroxidase mimicking activity which in turn helps selective naked eye detection of H_2O_2 and Hg^{2+} ions in solution. However, spectrophotometric detection limit goes down to 0.1 mM and 2.58×10^{-3} mM for H_2O_2 and Hg^{2+}, respectively. To contemplate peroxidase like activity, colorless 3,3',5,5' tetramethylbenzidine (TMB) is employed which in turn oxidized to a blue solution by H_2O_2 in presence of $ZnFe_2O_4$ rendering H_2O_2 sensing. It has been discovered that the blue color development is selectively held up by Hg^{2+} ion causing Hg^{2+} sensing possible. Judicious selection of Hg^{2+}ion once again indicates a strong affinity of nitrogen donor towards Hg^{2+}. This makes Hg^{2+} sensing possible without the use of any noble metal. A strong and definite '-N-Hg-N' binding interaction with nitrogen donors of TMB substrate causes blue color bleaching. Here we report the usefulness of an under-rated $ZnFe_2O_4$ nanoflower for the first time to detect Hg^{2+} spectrophotometrically and in a cost-effective way. On the other hand, highly mesoporous nanoflower has been shown to be a selective sensor for acetone also. Based on the above reaction/interaction strategies it is expected that the as-synthesized $ZnFe_2O_4$ NFs would stand to be a cost effective sensor material for biological application and environmental remediation.

Keywords: $ZnFe_2O_4$ NPs, TMB, peroxidase mimic, Hg^{2+}, acetone sensor.

INTRODUCTION:

Mercury ion (Hg^{2+}), particularly in aqueous medium is the most toxic among the heavy metals and it is a serious threat to for the advancement of human civilization.[1-2] Our ecosystem becomes contaminated with the Hg^{2+} ion due to the release of wastewater from the mining activities, municipal waste, combustion of oil and coal, manufacture of cement, combustion of sewage sludge, production of batteries, and others.[3-6] For drinking water, maximum concentration level is 2µg/L which has been standardized by U.S. Environmental Protection Agency (EPA).[2] Thus detection of Hg^{2+} is very much essential for aquatic life as well as human health. Till now various sensors have been developed for the detection of highly toxic Hg^{2+} using peroxidase-mimic property of the nanomaterials. But the materials used to develop those sensors are very expensive, because in most of the cases noble metals have been used as the sensors.[7-11] Thus synthesis of a cost effective Hg-sensor becomes a challenge to the researchers especially involving eco-friendly metal ions. Amongst various types of sensing methods, colorimetric sensing is useful to a large extent due to its simplicity and low cost.[12] Peroxidase reaction is an important type of redox reaction where enzyme oxidizes a specific substrate in the presence of peroxide.[13] Natural peroxides, like, Horseradish peroxidase (HRP) has some limitation to use, like suitable reaction condition, large scale application selectivity and stability.[13] For this purpose nanoparticles are brilliant alternatives and hence finds wider applicability.[14-17] Till now several metals, metal oxides, metal-metal oxide composites, metal ferrites graphene-nanomaterial composites have been used as a peroxidase mimicking material.[7-11,14-20]

Again, acetone has been used as a common solvent and extracting reagent in industry. It is also hazardous to human health mainly due to its higher dissolution power as solvent. Easy evaporation due to its high vapour pressure makes acetone concentration high (> 10,000 ppm) in air which causes several symptoms like, cephalalgia, nausea etc. Acetone is a biomarker for type-I diabetes (T1 D).[21] Noninvasive breath acetone detection has a significant role in diagnosis of diabetes and management of daily insulin injection.[22-23] As a result of this, acetone provides an alternative to the conventional standard blood analysis. Thus detection of acetone by a simple, cost effective technique has become a challenge to the researchers. Generally two methods, gas chromatography with flame ionization detection (FID) and selected ion flow tube mass spectrometry have been used to trace acetone. For this purpose metal oxide semiconductor based gas sensors are worthy of importance due to their cost effectiveness, easy preparation methods, high stability etc.[24-27]

$ZnFe_2O_4$ is an n-type semiconductor, having spinel structure. Due to the narrow band gap (1.86 eV) it has been used as the visible light sensitizer for the wide band gap semiconductor.[28] In recent days, due to the wide application in adsorption, photocatalysis, biosensing, solar cells etc. $ZnFe_2O_4$ has drawn the attention of the researchers.[29-34] Several techniques have been used to synthesize $ZnFe_2O_4$, such as, micro-emulsion, co-precipitation, hydrothermal, sol-gel, electrodeposition etc.[35-40] Generally ferrites (AFe_2O_4) (A= Ni, Zn, Co etc.) have some limitations to behave as a gas sensor because of their high temperature synthesis which makes them dense and reduce the surface area.[41] Till now several metal oxide semiconductors (SnO_2, ZnO, Co_3O_4, α-Fe_2O_3, CuO etc.) have been used as the gas sensors as well as biosensors depending on their morphologies.[12,42-44] One-dimensional nanostructures are widely used as gas sensors due to their

excellent response[45-51] In recent days some metal ferrites have also been used as the gas sensors as well as peroxidase mimic material.[52]

Here we have used a simple one pot synthetic route to prepare flower-like mesoporous gram quantity $ZnFe_2O_4$ under the modified hydrothermal (MHT) technique in a screw cap test tube. It has been synthesized via homogeneous precipitation of zinc and iron precursor compounds at 180 °C. No structure directing agents or stabilizers or capping agents have been used during the process which makes the $ZnFe_2O_4$ surface readily accessible by the incoming reactants in successive stages. Urea being highly soluble in water decomposes thereby under heat and hydrolyses metal ions and in turn removed without leaving any remnant along with the product. The as-synthesized material conveys the peroxidase mimicking activity as well as acetone gas sensing property. Then peroxidase mimicking reaction i.e., blue color formation step has been found to be halted selectively by Hg^{2+} ion which detect and quantify Hg^{2+} ion in aqueous solution. Thus the as-synthesized low cost material has three fold applications: peroxidase mimicking activity, Hg^{2+} ion and gas sensing capabilities.

EXPERIMENTAL SECTION:

Materials and Instruments: The related information is briefly discussed in the supporting information.

Synthesis of the nanoparticle:

To synthesize $ZnFe_2O_4$ NFs the following procedure has been adopted: Typically 0.14 g zinc sulfate (0.025 M) and 0.16 g anhydrous $FeCl_3$ (0.05 M) were dissolved in 20 mL distilled water and 0.3 g urea (0.25 M) was added to it. Then the whole solution was stirred for 10 min to make the solution homogeneous. Molar ratio of the Zn^{2+}: Fe^{3+}: urea was maintained as 1:2:4. The

solution turned brown in color. Next, the brown solution was transferred to the 20 mL screw capped test tube and was subjected to modified hydrothermal (MHT) reaction condition at 180 °C for 18 h. Subsequently, it was cooled to room temperature and the brick red colored mass was collected through centrifugation and washed with distilled water. Thereafter the product was annealed at 450°C for 3h in a muffle furnace. Finally it was cooled to room temperature and stored for characterization and for further use.

Detection of H_2O_2 using $ZnFe_2O_4$ NFs as peroxidase mimic:

A typical colorimetric experiment was performed as follows for catalytic oxidation of 3, 3', 5, 5' tetramethylbenzidine (TMB). First 25 µL methanolic solution (0.01 M) of TMB was taken along with 2 mL of 0.01 M acetate buffer (pH 4) and 500 µL of 1 mg mL^{-1} NF catalyst to make a solution. After that different concentrations of 30 % H_2O_2 solution (final concentrations of the individual solution are 9.5, 19, 28, 37, 55, 72, 90, 103, 126, 176, 373, 460 and 634 mM) were introduced to the catalyst containing solution. Final volume of the reaction mixture was made up to 3 mL. After 10 min of reaction time the resultant solution was analyzed using the UV-visible spectrophotometer withdrawing same amount of aliquot at a time.

To study the effect of TMB concentration the same procedure was followed keeping the final concentration of H_2O_2 fixed at 176 mM and using different concentration of TMB solution (final concentrations are 36, 54, 72, 90, 108, 143, 161, 213, 354, 517 and 678 mM). Final volume of the reaction mixture was maintained at 3 mL.

Detection of Hg^{2+}using $ZnFe_2O_4$ NFs as peroxidase mimic via colorimetric method:

An aliquot of 25 µL of 0.01 M TMB solution was taken with various concentrations of Hg^{2+} solution (2.5 to 100 µM) in 2 mL 0.01 M acetate buffer (pH 4). Then 500 µL 1 mg mL^{-1} catalyst and 250 µL ~ 0.2 M H_2O_2 was added sequentially into the TMB containing solution. After that the resultant aliquot was examined using UV- visible spectrophotometer.

Kinetic aspects of the peroxidase mimicking activity of $ZnFe_2O_4$ NFs:

Peroxidase mimicking activity of $ZnFe_2O_4$ has been studied using 3, 3', 5, 5' tetramethylbenzidine (TMB) as the peroxidase substrate in presence of H_2O_2. Kinetic study of the peroxidase mimicking activity of the as-synthesized NFs has been studied at ambient condition in acetic acid-sodium acetate buffer (0.01 M, pH 4.0). Kinetic measurements have been done by the change in absorbance at 652 nm using UV-vis spectrophotometer. The as-obtained data are fitted into the Michaelis-Menten equation. The useful reactions with equations for kinetic measurements have been incorporated in the supporting information.

Gas sensor device fabrication and sensor set up:

A detailed study for the fabrication and set up of gas sensor device has been discussed in the supporting information.

Results and Discussion:

Here we have reported the synthesis of hierarchical flower-like $ZnFe_2O_4$ via our laboratory developed MHT technique at ~180° C for 18 h. We have used anhydrous $FeCl_3$, $ZnSO_4$, $7H_2O$ as precursor compounds and urea as a hydrolyzing agent. Small ‘bite’ of urea presumably cannot

serve the purpose of a capping agent for the particles under prolong heat. Under the experimental condition, urea decomposes in water and from there hydroxide ion (OH^-) hydrolyzes Fe^{3+} and Zn^{2+} ions. Then under MHT condition metal hydroxides suffer dehydration and produce $ZnFe_2O_4$. Judicious employment of urea causes homogeneous precipitation of $ZnFe_2O_4$. Ammonia is generated that causes hydrolysis of metal ions. After 18 h of heating, a brick red product separates out as an insoluble mass that show up the flower-like morphology. Even after annealing the NFs, the parental flowery morphology has been found to be retained. Finally the product, after repetitive washing and drying, was annealed at 450 °C as mentioned earlier to make the product crystalline. The morphology of $ZnFe_2O_4$ changes drastically as we employ alkaline (NaOH) or acidic (HCl) conditions (Figure S3). The NaOH addition localised several yellowish tinges onto the surface of the precipitate indicating selective leaching of Fe^{3+} from $ZnFe_2O_4$ which is confirmed from the FTIR spectra (Figure S4). In the synthetic protocol we did not use any surfactant or organic compound as the structure directing agent for the synthesis of hierarchical nanoflower. The as-synthesized nanoflower has been used both as a sensor material for Hg and acetone gas sensing. Figure 1(a) demonstrates the XRD spectra of the as-synthesized nanoflower after annealing at 450 °C. The XRD pattern of the as-synthesized nanoflower ascribes to the spinel $ZnFe_2O_4$ (JCPDS, No.79–1150).[53] The diffraction peaks of $ZnFe_2O_4$ around 30.1°, 35.2°, 42.8°, 53.1°, 56.5° and 62.3° stand for the crystal plane (220), (311), (400), (422), (511) and (440), respectively. For further confirmation of the crystalline nature of the as-synthesized $ZnFe_2O_4$, we have performed the Rietveld refinement analysis. The Rietveld refinement of the XRD pattern (Figure 1b), using FULLPROF[54] confirms the single phasic nature of the nanoflower. This $ZnFe_2O_4$ crystallizes in a cubic structure under the space group

Fd-3*m*. The lattice parameters are determined as, $a=b=c=8.424(4)$ Å. From figure 1b it is observed that intensities and positions of the calculated and observed peaks are same.

The composition of the material has been confirmed from the FTIR spectrum of the as-synthesized material (figure 1(c)). The peak around ~3470 cm^{-1} and ~1640 cm^{-1} relates to the water of hydration.[55] The high frequency band at ~550 cm^{-1} corresponds to the Fe-O stretching vibration and low frequency band at ~435 cm^{-1} is assigned to the Zn-O stretching vibration,[56] altogether which confirm the successful synthesis of $ZnFe_2O_4$. Peak at 1127 cm^{-1} arises due to overtones.[55]

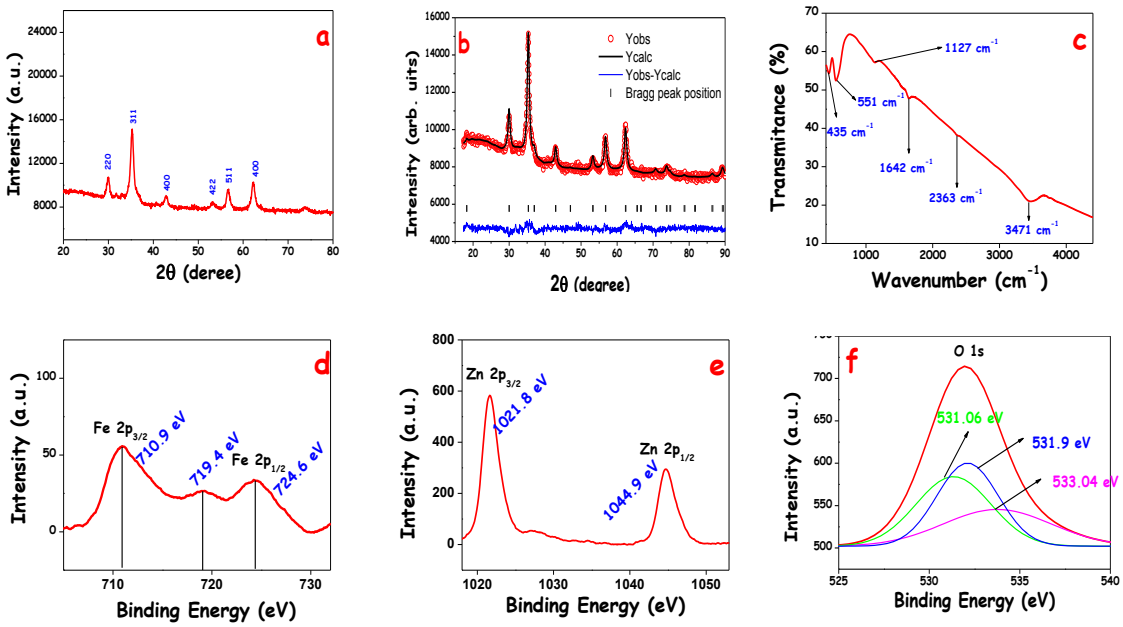

Figure 1: XRD spectra (a), Reitveld refinement spectra (b) and FTIR spectra (c) of $ZnFe_2O_4$ NPs. Fe 2p (d) and Zn 2p (e) and O 1s (f) XPS of $ZnFe_2O_4$ NFs.

In order to confirm the oxidation state of the elements present in the as-synthesized material XPS analysis has been performed (figure 1d,e,f). Figure 1d exhibits that $Fe_{3/2}$ section is divided into

two peaks of binding energy 712.4 eV and 710.9 eV. This splitting recommends that Fe^{3+} present in two chemical states (A sites and B sites).[53] This may be due the presence of Fe^{3+} in two different coordination environments in the spinel structure, tetrahedral site and octahedral site. Binding energy at 712.42 eV and 710.9 eV stand for the tetrahedral site and octahedral site, respectively. Binding energy at around 719.4 eV is for the shakeup satellite peak for the octahedral site and tetrahedral site and the peak at 724.6 eV is for $Fe_{1/2}$.[57] In figure 1e peak at 1021.8 eV and 1044.9 eV demonstrate the binding energy for the $Zn_{3/2}$ and $Zn_{1/2}$, respectively. Figure 1f demonstrates the broad asymmetric curve for O 1s. After deconvoluting we have got three distinct peaks which are at 531.06 eV, 531.9 eV and 533.04 eV. The most intense peak which illustrates the presence of the lattice oxygen in metal oxide framework has been situated at 531.9 eV. The other two peaks at 531.06 eV and 533.04 eV designate the presence of other oxygen containing group, such as, OH, H_2O and carbonate group. The discussion confirms that the as-synthesized material is $ZnFe_2O_4$ with NF morphology.

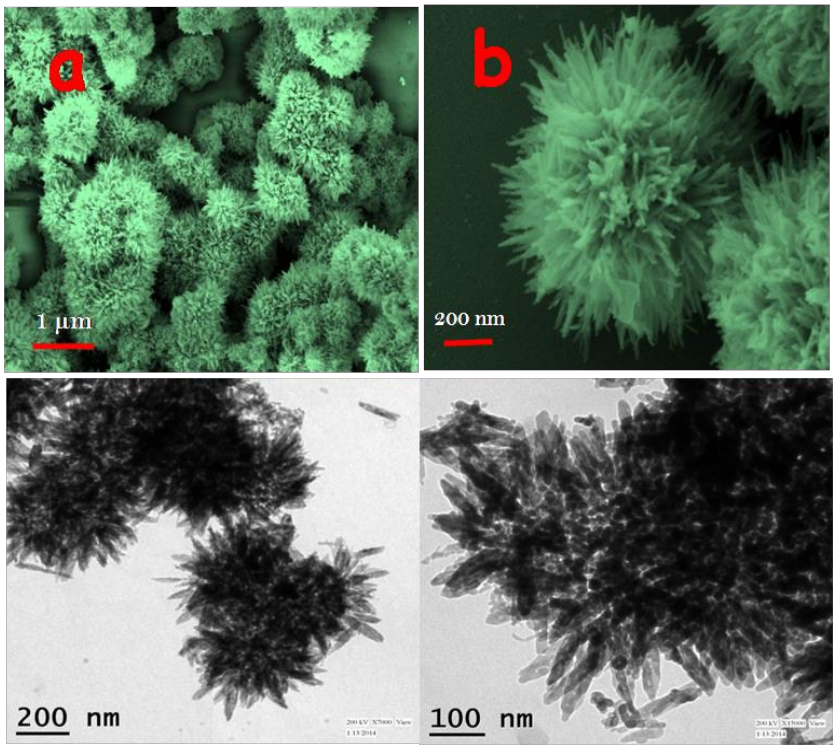

Figure 2: Low magnification (a, c) and high magnification (b, d) FESEM and TEM images of $ZnFe_2O_4$ NFs, respectively.

Morphology of the as-synthesized $ZnFe_2O_4$ has been examined by FESEM and TEM analysis. Figure 2a,b display the FESEM images of as-synthesized $ZnFe_2O_4$, in lower and higher magnification, respectively. It has been observed from figure 2a,b that $ZnFe_2O_4$ has acquired 3D flowerlike morphology. Figure 2c,d demonstrate the TEM images of 3D $ZnFe_2O_4$. Highly magnified TEM image (figure 2d) of $ZnFe_2O_4$ reveals that the development of 3D flowerlike morphology is due to the self-assembly of 1D nanorods and occurred in presence of $ZnSO_4$. The length and diameter of the individual nanorods are ~ 104 nm and ~ 27 nm, respectively. One interesting autocatalytic 3D structure directing motif of ZnO has been observed here, while $FeCl_3$ and $ZnSO_4$ were subjected to MHT reaction in presence of urea (Scheme 1).

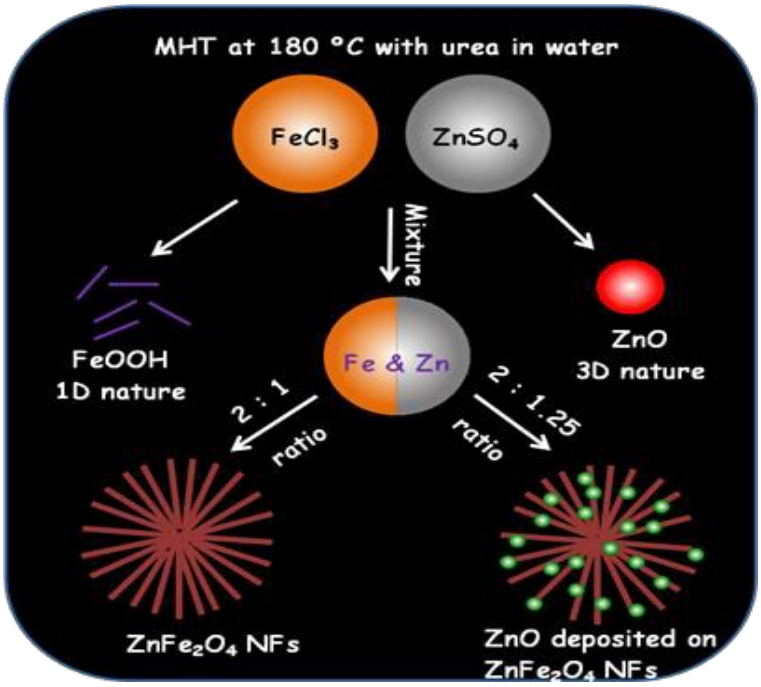

Scheme 1: Pictorial presentation of synthetic strategy of the as-synthesized materials at different reaction condition.

This has been indirectly confirmed unequivocally while only $FeCl_3$ was used as the lone precursor under the experimental condition; only 1D nanorod morphology was obtained (Figure S2). So under the MHT experimental condition, $Fe(OH)_3$ dehydrates to ferric oxo-hydroxide (FeOOH) species. In successive stages with time habitual 1D growth of FeOOH takes place which appears as nanorods. Even for lone $Fe(OH)_3$ case, there the assembly of FeOOH nanorods was not observed. Interestingly, only after the incorporation of $ZnSO_4$ into the reaction mixture i.e., together with $ZnSO_4$, assembly of the nanorods started (figure 3) to grow. At a particular molar ratio of Zn and Fe (Fe:Zn = 2:1) the as-synthesized product attained its perfect 3D flower-like morphology. Figure 3 displays the FESEM images of the as-synthesized product at different Fe and Zn molar ratio. At low concentration of $ZnSO_4$, assembling of nanorods started (figure 3b) and it gradually gained its hierarchical structure with increase in $ZnSO_4$ concentration. Again at high concentration of $ZnSO_4$ spherical ZnO, a product of $Zn(OH)_2$ dehydration, deposited over the hierarchical flower-like $ZnFe_2O_4$ (figure 3f) morphology. Thus ZnO plays its inherent motif for 3D structure directing capability.[58] To conclusively prove the role of SO_4^{2-}, we have followed the same experimental procedure but with $Zn(CH_3OO)_2$ and $ZnCl_2$ separately as precursor (in two different sets), instead of $ZnSO_4$. In both the cases we did not get any flower like morphology (Figure S5). Thus the importance of SO_4^{2-} has a bearing for the development of well defined but reproducible morphology of the nanomaterials, $ZnFe_2O_4$.[59] During the optimization of the reaction condition we have tried the synthesis of the nanomaterial in a time dependent fashion. It has been observed that 18 h time at 180℃ was optimum. The flower like growth is presumably slow and requires long time. Less time and lower temperature caused ill defined morphology evolution for $ZnFe_2O_4$ (Figure S6).

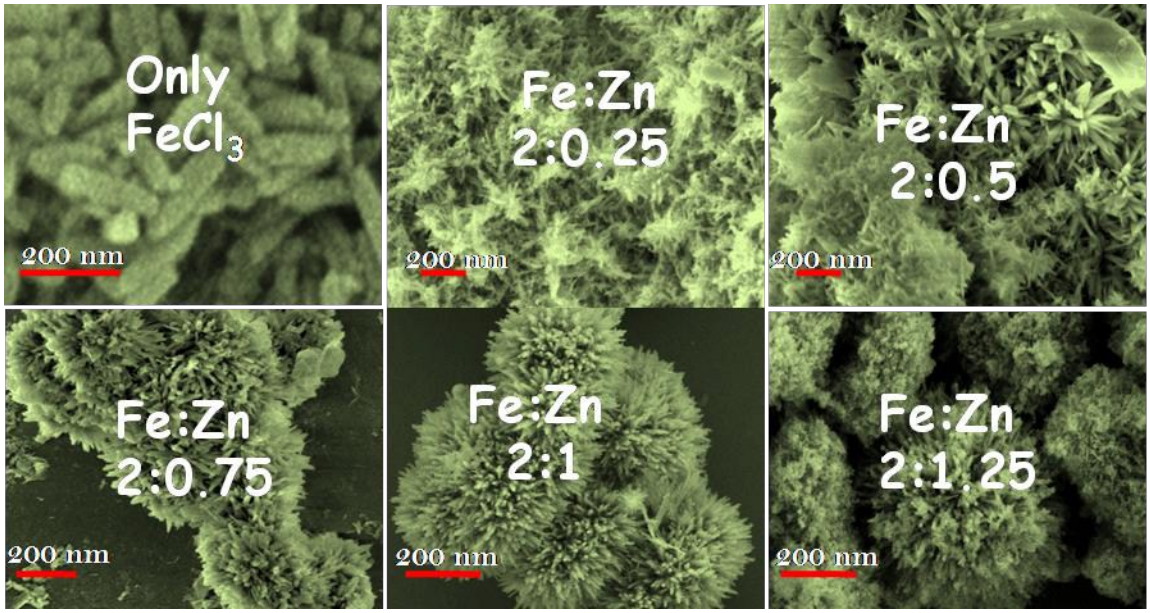

Figure 3: FESEM images of $ZnFe_2O_4$ at different molar ratio of Fe and Zn.

Figure S7 illustrates EDX of the as-synthesized product where we can see that the product consists of Fe, Zn and O as the elemental composition. Figure 4 demonstrates the elemental line mapping of FESEM image of the as synthesized product which conveys the atomic composition of elements (Fe : Zn = 2 : 1). It has been observed that the flower-like morphology was intact even after annealing at 450 °C i.e. the as-synthesized $ZnFe_2O_4$ is robust in nature.

In order to investigate the porous nature of the as-synthesized product, N_2 adsorption-desorption isotherm analysis has been done. Figure 5a illustrates the N_2 adsorption-desorption isotherm of the sample, studied at 72 K temperature from 0.1 to 1 P/P_0 range. The graph presented in Figure 5a conveys that the N_2 adsorption-desorption isotherm follows type IV category and the calculated Brunauer-Emmett-Teller (BET) surface area is 70.274 m^2/g. According to the pore size distribution curve (figure 5b) the pore width of the material is 2.4 nm i.e. the flower-like robust $ZnFe_2O_4$ NF is mesoporous (2-50 nm) in nature. In the figure 5b it has been shown that

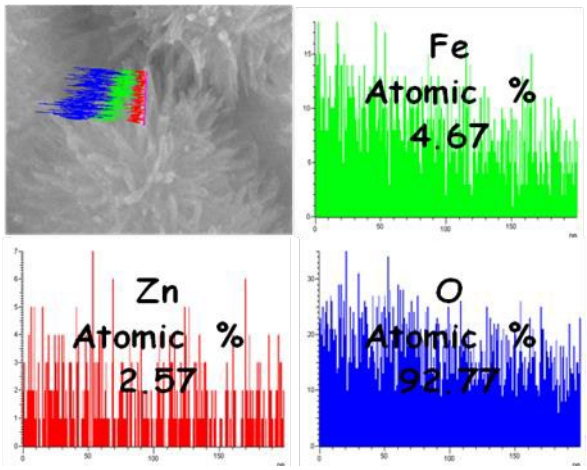

Figure 4: Elemental line mapping of the FESEM image of $ZnFe_2O_4$ NFs.

the pores are highly uniform with narrow size distribution. Here pores are nothing but the interspaces of the crosslinked 1D nanorods which was generated might be during the self-assembling of the same. This high specific surface area and uniform pore size distribution makes $ZnFe_2O_4$ a good adsorbent for the acetone as well as TMB. The porous nature of 3D flower-like assembly is an outcome of the oriented attachment process of the in-situ produced two (Fe and Zn) oxide materials as a matter of successive but slow (18 h MHT reaction) attachment procedure.

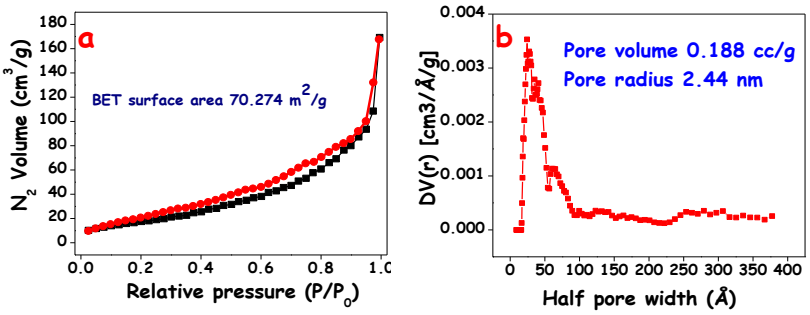

Figure 5: (a) N_2 adsorption-desorption isotherm plot and (b) pore size distribution curve of $ZnFe_2O_4$ NFs.

The catalytic activity:

The catalytic activity of the as-synthesized NF material has been demonstrated in this manuscript through the catalytic oxidation of 3, 3´, 5, 5´ tetramethylbenzidine (TMB) in presence of H_2O_2 (figure 6a). Using this peroxidase mimic activity of $ZnFe_2O_4$ quantitative detection of toxic metal

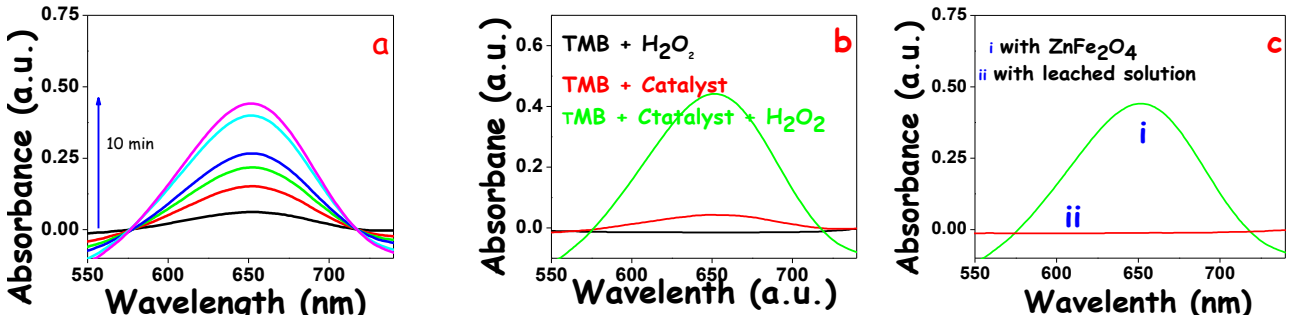

Figure 6: (a) UV-vis absorption spectra of TMB oxidation with respect to time, (b) Absorption spectra of TMB oxidation at different reacting condition (control experiment) and (c) Absorption spectra of TMB oxidation with crystalline $ZnFe_2O_4$ (i) and its leached ions (ii).

(Hg^{2+}) has been performed. Several control reactions have been done to study the behavior of catalytic oxidation of TMB by $ZnFe_2O_4$ (figure 6b). It has been observed that in presence of both H_2O_2 and $ZnFe_2O_4$ intense blue colored solution was observed, but in absence of H_2O_2 or $ZnFe_2O_4$ colorless solution was observed. This observation signifies that the following reaction is catalyzed by the $ZnFe_2O_4$ NPs and here $ZnFe_2O_4$ exhibits enzyme like activity. During the reaction, H_2O_2 first physisorb on the porous $ZnFe_2O_4$ surface. These adsorbed H_2O_2 converts to $OH^{\cdot}$ by the Fe^{3+} (Fenton reaction) ion in the $ZnFe_2O_4$.[60]

$$Fe^{3+} + H_2O_2 \longrightarrow Fe^{2+} + OOH^{\cdot} + H^{+}; \quad Fe^{2+} + H_2O_2 \longrightarrow Fe^{3+} + OH^{-} + OH^{\cdot}$$

Due to the high surface area of $ZnFe_2O_4$, Fe^{3+} site is more exposed towards the H_2O_2 and thus easily $OH^{\cdot}$ produces which enhances the catalysis.

A schematic diagram of the catalytic oxidation of TMB has been manifested in Scheme S1.

It is very much essential to nullify the probability of the catalytic oxidation of TMB by ions leached out from the $ZnFe_2O_4$, instead of crystalline $ZnFe_2O_4$. For this purpose 2 mg of $ZnFe_2O_4$ was incubated for 2 h and then centrifuged. After that same experimental procedure (as per demonstrated in H_2O_2 detection part) was followed taking 500 µL of the centrifuged solution as the catalyst. Figure 6c attributes the catalytic activity by the crystalline $ZnFe_2O_4$ and leached ion from the $ZnFe_2O_4$ and comparing these two it can be established that the catalytic activity is due to the crystalline $ZnFe_2O_4$, not due to its leaching ions.

It is already reported that peroxidase mimic activity of NPs is dependent on the pH of the solution, temperature and concentration of H_2O_2.[32,7-11,14-20] In order to investigate the effect of pH and the concentration of H_2O_2 we performed the experiment at different pH (pH 3.8 to 8) (figure 7a) and at different H_2O_2concentrations (figure 7b). The whole experimental study has been done at room temperature. In figure 7a we see that the $ZnFe_2O_4$ becomes more reactive at pH 4.0. Figure 7b exhibits that activity of the reaction gradually increases with increase in H_2O_2 concentration and gets equilibrium at 176 mM of concentration. Thus, pH 4.0 and 176 mM of H_2O_2 concentration were set as the optimal condition for the catalytic study. Here based on the peroxidase-mimic activity of $ZnFe_2O_4$ a colorimetric experiment has been developed to detect H_2O_2. From figure 7b it is clear that with increase in H_2O_2 concentration, oxidation of TMB increases i.e. oxidation of TMB is proportional to the H_2O_2 concentration. Thus it is very quite straight forward to detect H_2O_2 using spectrophotometeric method (λ = 652 nm). Inset of figure

7b illustrates a H_2O_2 calibration curve ranging from 28 mM to 176 mM with limit of detection (LOD) ~ 0.1 mM.

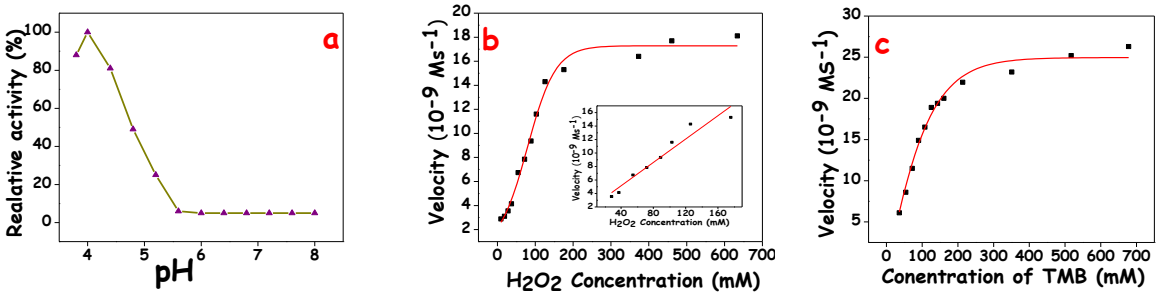

Figure 7: (a) pH dependence, (b) H_2O_2 concentration dependence and (c) TMB concentration dependence of $ZnFe_2O_4$ NFs for TMB oxidation.

Kinetic analysis:

In order to calculate the kinetic parameters of the $ZnFe_2O_4$ NPs catalyzed peroxidase-mimic reaction, the catalysis has been done with different H_2O_2 and TMB concentration (figure 7b and 7c). According to the change in absorbance intensity at λ = 652 nm after 10 min the characteristic Michaelis-Menten curves were plotted for both the substrates, H_2O_2 and TMB (figure 8a and 8b, respectively). From the Lineweaver-Burk plot (figure 8a and 8b), Michaelis-Menten constant (K_m) and maximum initial velocity i.e. rate of the reaction (V_{max}) were obtained for the substrates. The absorbance values were converted to concentration by Lambert-Beer law using molar absorption coefficient (ε) of 39000 L $M^{-1}cm^{-1}$ for TMB solution.[13]

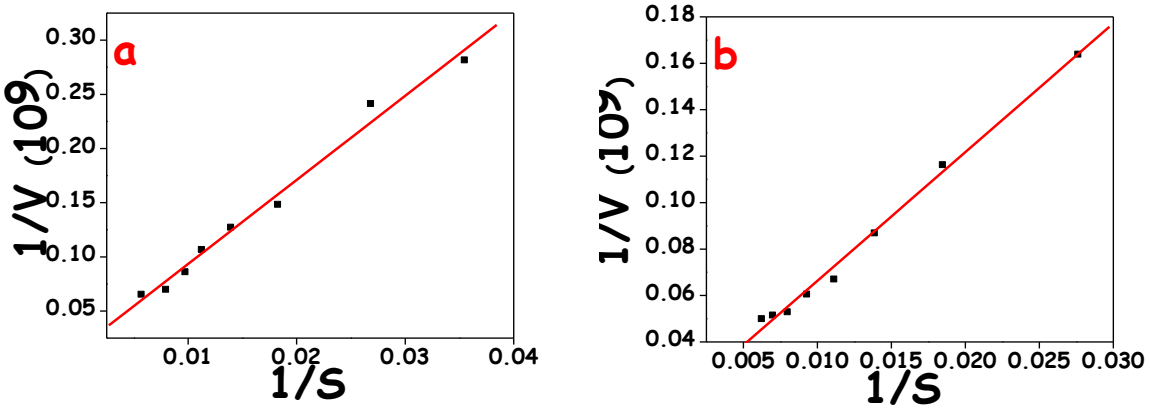

Figure 8: Lineweaver-Burk plot for $ZnFe_2O_4$ (a) varying H_2O_2 concentration keeping TMB concentration fixed and (b) varying TMB concentration keeping H_2O_2 concentration fixed.

Michaelis-Menten constant declares the affinity of the enzyme with the substrate. In the table 1, it is shown that for the as-synthesized $ZnFe_2O_4$ K_m value is lower than the reported $ZnFe_2O_4$ and higher than the HRP for TMB solution.[32] This high affinity of the as-synthesized $ZnFe_2O_4$ towards TMB with respect to HRP may be due to the sharp needle like 1 D structure of the NPs.

Catalyst	Substrate	K_m/mM	$V_{max}/10^{-8}$ M s^{-1}
HRP[32]	TMB H_2O_2	0.434 3.7	10 8.71
$ZnFe_2O_4$ NPs[32]	TMB H_2O_2	0.85 1.66	13.31 7.74
$ZnFe_2O_4$ NPs (this work)	TMB H_2O_2	0.509 490.72	9.18 6.32

Table 1: Comparison of kinetics parameters of different reported material with the as-synthesized $ZnFe_2O_4$ NFs.

Detection of Hg^{2+}:

Hg^{2+} generally stimulates the oxidation of TMB substrate in peroxidase or oxidase like reaction when nanoparticles are used as the oxidase or peoxidase mimic materials.[7-11] For the detection of Hg^{2+}, researchers generally use very expensive noble metals such as Ag, Pt and Au.[7-9] Here we have used $ZnFe_2O_4$ nanoflower to detect Hg^{2+}. In this study it is observed that Hg^{2+} inhibits the oxidation of TMB substrate by H_2O_2 in presence of low cost $ZnFe_2O_4$. It was observed that with increase in Hg^{2+} the intensity of the blue color become faint and at a particular concentration no

blue color was observed. Which signifies that there remains no free TMB (all are bound to Hg). Figure S8 represents that with the increase in Hg^{2+} concentration the absorbance value for ox-TMB gradually decreases. Scheme 2 represents the pictorial presentation of TMB oxidation and it's inhibition in presence of Hg^{2+}.

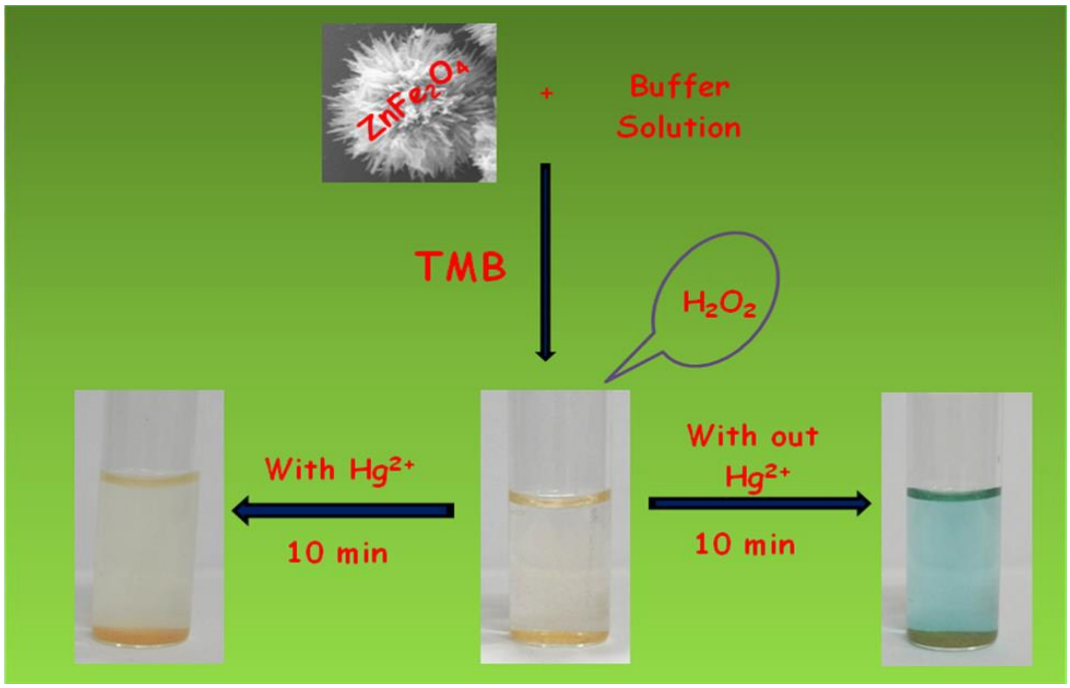

Scheme 2: Schematic presentation of oxidation and inhibition of TMB by $ZnFe_2O_4$ NFs in absence and in presence of Hg^{2+} ion.

The inhibition effect of Hg^{2+} concentration on TMB oxidation has been illustrated in figure 9a. Figure 9b depicts the linear calibration plot, linear range is from 0 to 10×10^{-6} M). The LOD (limit of detection) for Hg^{2+} is 2.58×10^{-3} mM. LOD is expressed as $3\sigma/k$, where σ is the standard deviation of the blank sample and k is the slope of the analytical calibration.[13] A series of metal ions, such as, Cd^{2+}, Pb^{2+}, Cu^{2+}, Cr^{3+}, Mn^{2+}, Zn^{2+} were made involved to taste their

inhibitory effect. Figure 9c illustrates that besides Hg^{2+} no other metal ions under examination have the ability to inhibit the oxidation of TMB substrate.

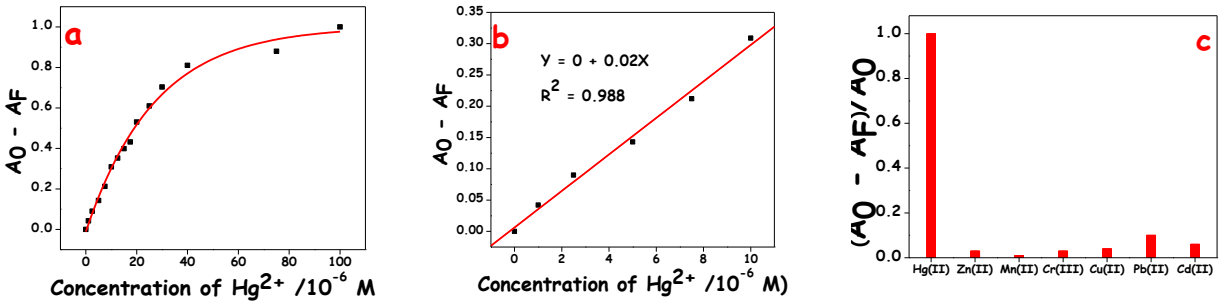

Figure 9: (a) Graphical presentation of effect of Hg^{2+} concentration on TMB concentration (A_0 is the initial absorbance value, A_F is the absorbance value at different Hg^{2+} ion concentration, (b) linear plot of the same and (c) Response of different metal ions on inhibition of TMB oxidation).

The selectivity of Hg^{2+} towards TMB provides a simple colorimetric method to detect Hg^{2+}. During the experiments it was observed that as soon as Hg^{2+} has come in contact with TMB a yellowish-white color was generated and disappeared instantly. From this observation we conclude that Hg^{2+} forms a complex with TMB substrate. It is reported that substrate containing nitrogen centre has strong affinity towards Hg^{2+} ion.[7,61,62] Hg^{2+} generally forms strong covalent bond with nitrogen. In our case the possible binding centre are terminal amine group ($–NH_2$) of two TMB substrates and Hg^{2+}. Now we can explain the scenario of figure S8, as Hg^{2+}increases in the reacting solution, TMB forms complex with Hg^{2+}. Thus number of effective TMB molecules to be oxidized by the H_2O_2 in presence of zinc ferrite becomes less. As a matter of fact absorbance in figure S8 decreases with increase in Hg^{2+} concentration. The probable reaction could be as follows:

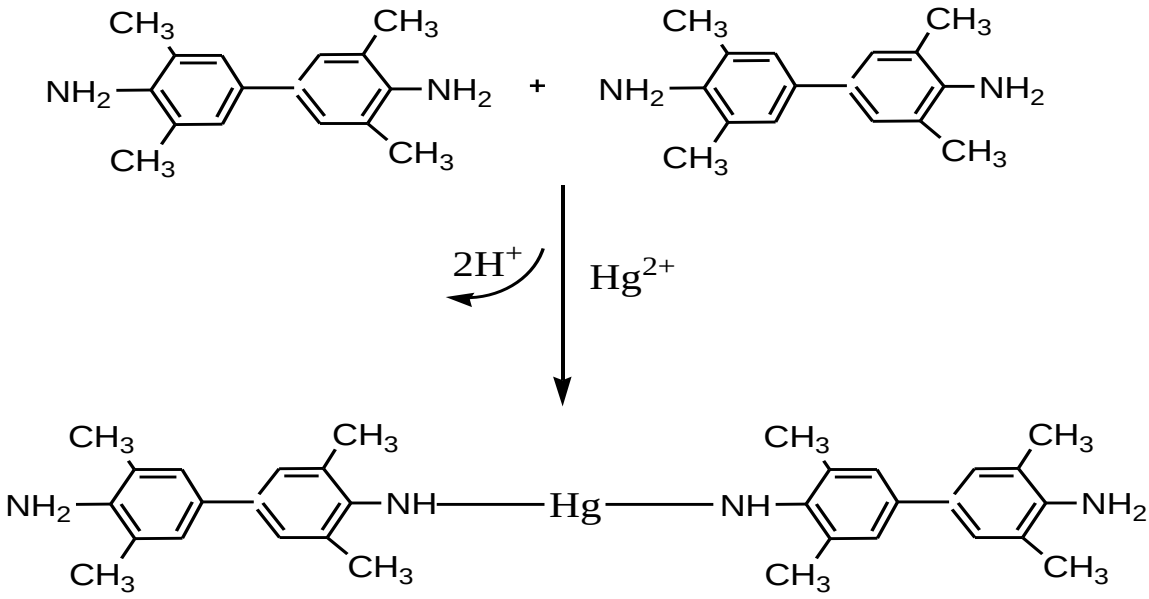

Scheme 3: Formation of complex of Hg^{2+} with TMB.

Gas sensing:

As the synthesized $ZnFe_2O_4$ NFs exhibits good N_2 adsorption-desorption profile (figure 5a), we have tried to fabricate it as a gas sensor for the selective detection of acetone. For this purpose here gas sensing measurements of zinc ferrite were performed in presence of acetone, ethanol and hydrogen (H_2). In this work the response is defined by the following equation:

$$S = \frac{R_a}{R_g} \qquad (1)$$

Where, S is the response R_a and R_g are the resistances of sensing layer in synthetic air and vapours, respectively.

It is well known that the sensor response has strong dependence on working temperature. For that the sensor was tested at 2000 ppm of acetone as a function of temperature to obtain the maximum response temperature, exhibited in figure 10 a. The sensor response showed increase-

maximum- decrease trend. Maximum response temperature was found to be 300°C. The dynamic response at different concentrations measured at 300°C is presented in figure 10b. The analyte vapor was ON for 5 minutes to obtain the maximum response and then the gas was OFF for 10 minutes to return back to the baseline resistance. The sensing response was found to be 36.5 – 100 times for the concentration of 1100 – 8800 ppm of acetone. The responses of different nanostructured zinc ferrite towards acetone are presented in table 2. It was observed from the table that apart from Zhou et al.[63] our sensor showed better response than others reported results.[64-66]

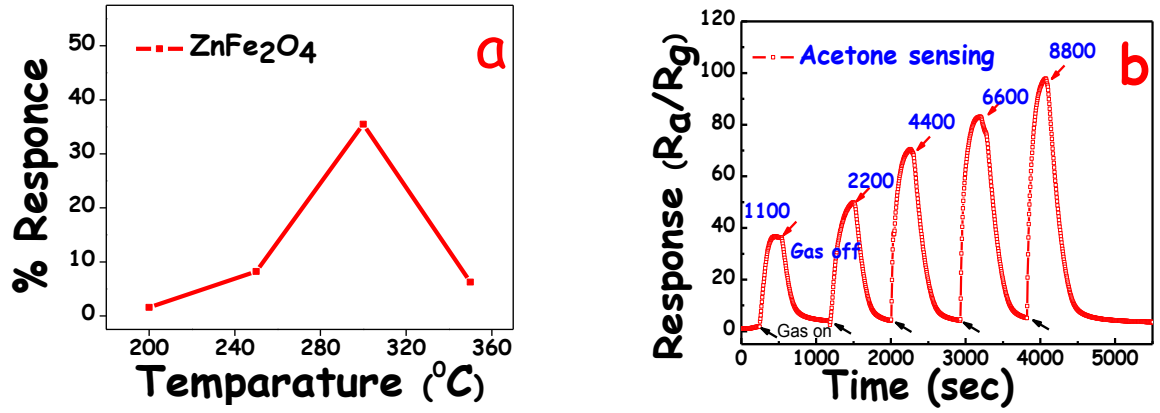

Figure 10: Graphical presentation of gas sensing response of $ZnFe_2O_4$ at different temperature keeping concentration fixed (a) and at different concentration keeping temperature fixed (b).

Structure of Zinc Fettite	Acetone concentration (ppm)	Operating Temperature (°C)	Response (R_a/R_g)	References
Porous nanospheres	100	200	42	63
Nanotubes	1000	300	18.5	64
Nanoparticles	1000	350	16.8	64
Nanoparticles	500	300	20	65
Nanoparticles	50	270	4.2	66
Nanoflower	1100	300	36.5	This work

Table 2: List of different reported zinc ferrite nanostructures and their gas sensing capabilities.

The selectivity measurements were also performed in presence of acetone, ethanol and H_2 at 1000 ppm and has been shown in Figure 11. It was found that the iron ferrite is more selective towards acetone compared to ethanol and H_2 which is also in agreement with Zhou et al.[62]

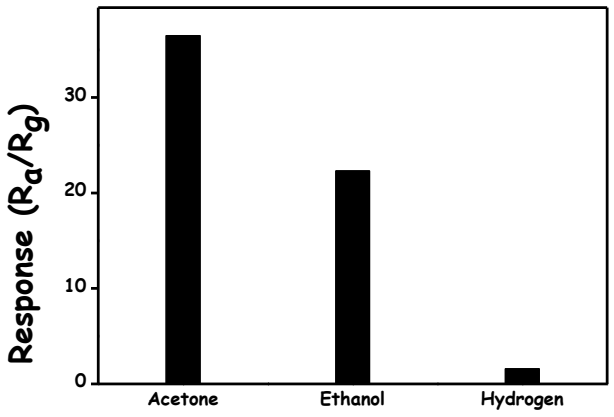

Figure 11: Selectivity of $ZnFe_2O_4$ NFs for acetone sensing over ethanol and hydrogen.

Gas sensing mechanism

The gas sensing mechanism of zinc ferrite sensors can be illustrated by the modulation model of depletion layer,[67] which has been shown in scheme 4. The sensing property of a material has been quantified by measuring the change in resistance of the material at different gas environment. Resistance has been changed mainly due to the adsorption and desorption of gas molecules on the surface of the sensor.[63-66] When the zinc ferrites are exposed to air the oxygen molecules are physisorbed on the surface of the material. The physisorbed oxygen species trap the electrons from the conduction band of the zinc ferrite and became the O_2^-, O^-, O^{2-} ion depending on the working temperature (Eq. 4 – 7).

$$O_{2(g)} \rightarrow O_{2(ads)} \quad (2)$$

$$O_{2(ads)} + e^- \rightarrow O_{2(ads)}^- \quad (3)$$

$$O_{2(ads)}^- + e^- \rightarrow 2O_{(ads)}^- \quad (4)$$

$$O_{(ads)}^- + e^- \rightarrow O_{(ads)}^{2-} \quad (5)$$

Hence oxygen molecules act as electron acceptors which lead to the formation of thick charge layer on the surface which increases the potential barriers shown in scheme 4. Thus the material eventually exhibits high resistance towards carrier mobility. At this condition, when these zinc ferrite sensor is exposed to reducing gases or vapours like acetone, ethanol and hydrogen at high temperature, the chemisorbed oxygen species will react with the gases by the following reaction.

$$C_3H_6O + 8O^- \rightarrow 3CO_2 + 3H_2O + 8e^- \quad (6)$$

$$CH_3CH_2OH + 6O^- \rightarrow 2CO_2 + 3H_2O + 6e^- \quad (7)$$

$$H_2 + O^- \rightarrow H_2O + e^- \quad (8)$$

Like so, the electrons will return back to conduction band of $ZnFe_2O_4$ which reduces the potential barrier and thus carrier concentration increases. As a result the resistance of the materials will decrease.

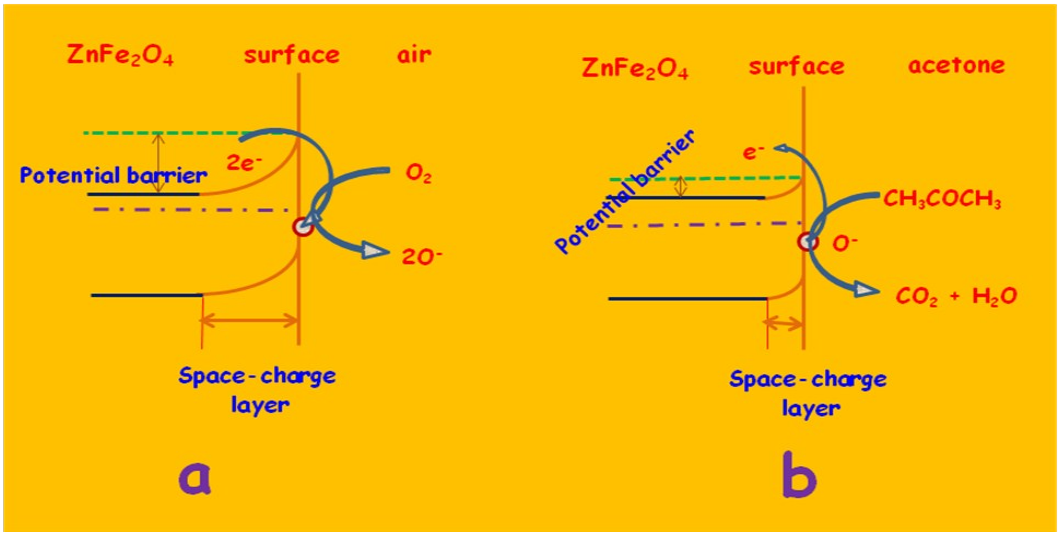

Scheme 4: Schematic presentation of probable gas sensing mechanism of $ZnFe_2O_4$ at two different gas environments (here, acetone and air).

This high efficiency in gas sensing property of the crystalline flower-like $ZnFe_2O_4$ compared to the reported zinc ferrites (table 2) can be explained by the following way. All the nanoflowers are interconnected through their randomly oriented 1D nanowires which make them porous. Thus this 3D hierarchical nanostructure affords a high surface-to-volume ration. As a result more gas molecules adsorb and desorb on/from the $ZnFe_2O_4$ surface which makes it an efficient gas sensor.

CONCLUSION:

In conclusion, we demonstrate a one pot, large scale synthesis of 3D porous $ZnFe_2O_4$ NFs. During the preparation of this nanomaterial no surface directing agent was used. The as-synthesized material becomes important for naked eye detection of H_2O_2 and Hg^{2+} ion in aqueous solution. However, the detection sensitivity goes down to 0.1 mM for H_2O_2 and 2.58×10^{-3} mM for Hg^{2+} while spectrophotometry was used. Eventually, $ZnFe_2O_4$ becomes the first reported oxide based material which finds a spectrophotometric application for Hg^{2+}detection. Furthermore, acetone vapor sensing makes the morphologically $ZnFe_2O_4$ NF important. Due to the high surface area of $ZnFe_2O_4$, it stands as a better and selective acetone gas sensor material in comparison to the other reported zinc ferrites. Thus, the present work provides a low cost sensor material from MHT for practical use and also becomes sturdy platform for the development of cost effective gas sensor.

Acknowledgements: The authors are thankful to Prof. Rabibrata Mukherjee, Department of Chemical Engineering, IIT Kharagpur for BET measurement. S. Santra acknowledges DST for Ramanujan Fellowship (project no. SR/S2/RJN-104/2011). We are also thankful to DST and CSIR, New Delhi, India for financial assistance, and the Indian Institute of Technology, Kharagpur for financial and instrumental support.

Supporting Information: Materials and instruments, gas sensor device fabrication and sensor set up. Michaelis-Menten equation and Linewaver-Burk plot, FESEM and TEM image of FeO(OH), FTIR of leached ion, EDX of $ZnFe_2O_4$. Absorption spectra of TMB oxidation at different Hg^{2+} concentrations.

References:

1. J. Wang, B. Deng, H. Chen, X. Wang and J. Zheng, *Environ. Sci. Technol.,* 2009, **43**, 5223.

2. F. He, W. Wang, J. W. Moon, J. Howe, E. M. Pierce and L. Liang, *ACS Appl. Mater. Interfaces*, 2012, **4**, 4373.

3. E. G. Pacyna and J. M. Pacyna, *Water Air Soil Pollut.*, 2002, **137**, 149.

4. K. H. Nam, S. Gomez-Salazar and L. L. Tavlarides, *Ind. Eng. Chem. Res.,* 2003, **42**, 1955.

5. Q. Wang, D. Kim, D. D. Dionysiou, G. A. Sorial and D. Timberlake, *Environ. Pollut.,* 2004, **131**, 323.

6. J. Aguado, J. M. Arsuaga and A. Arencibia, *Ind. Eng. Chem. Res.,* 2005, **44**, 3665.

7. N. Kanayama, T. Takarada and M. Maeda, *Chem. Commun.*, 2011, **47**, 2077.

8. J. Liu, X. Hu, S. Hou, T. Wen, W. Liu, X. Zhu and X. Wu, *Chem. Commun.*, 2011, **47**, 10981.

9. G. W. Wu, S. B. He, H. P. Peng, H. H. Deng, A. L. Liu, X. H. Lin, X. H. Xia and W. Chen, *Anal. Chem.,* 2014, **86**, 10955.

10. A. Chaudhary, A. Gupta and C. K. Nandi, *RSC Adv.*, 2015, **5**, 40849.

11. G. L. Wang, X. F. Xu, L. H. Cao, C. H. He and Z. J. Li, Zhang, C. *RSC Adv.* **2014**, *4*, 5867.

12. W. Qin. L. Su, C. Yang, Y. Ma, H. Zhang and X. Chen, *J. Agric. Food Chem.,* 2014, **62**, 5827.

13. C. Ray, S. Dutta, S. Sarkar, R. Sahoo, A. Roy and T. Pal, *J. Mater. Chem. B*, 2014, **2**, 6097.

14. Y. Fan and Y. Huang, *Analyst*, 2012, **137**, 1225..

15. W. Chen, J. Chen, Y. B. Feng, L. Hong, Q. Y. Chen, L. F. Wu, X. H. Lin and X.H. Xia, *Analyst*, 2012, **137**, 1706.

16. T. Lin, L. Zhong, L. Guo, F. Fu and G. Chen, *Nanoscale*, 2014, **6**, 11856.

17. K. Zhang, W. Zuo, Z. Wang, J. Liu, T. Li, B. Wang and Z. Yang, *RSC Adv.*, 2015, **5**, 10632.

18. C. Wang, J. Zhu, S. Liang, H. Bi, Q. Han, X. Liu and X. Wang, *J. Mater. Chem. A*, 2014, **2**, 18635.

19. Y. Peng, Z. Wang, W. Liu, H. Zhang, W. Zhou, H. Tang, F. Chen and B. Wang, *Dalton Trans.*, 2015, **44**,

12871.

20. S. Dutta, S. Sarkar, C. Ray and Pal, T. *RSC Adv.*, 2013, **3**, 21475.

21. C. Turner, C. Walton, and S. Hoashi, and M. Evans, *Journal of Breath Research*, 2009, **3**, 046004.

22. C. Wang, A. Mbi and M. A. Shepherd, *IEEE Sens. J.*, 2010, **10**, 54.

23.W. Q. Cao, Y. X. Duan, W. Cao and Y. Duan, *Crit. Rev. Anat. Chem.* 2007, **37**, 3.

24. X. Li, W. Wei, S. Wang, L. Kuai, and B. Geng, *Nanoscale*, 2011, **3**, 718.

25. Q. Simon, D. Barreca, A. Gasparotto, C. Maccatto, E. Tondello, C. Sada, E. Comini, A. Devi and R. A. Fischer, *Nanotechnology*, 2012, **23**, 025502.

26. P. Sun, Y. Liu, X. Li, Y. Sun, X. Liang, F. Liu, *RSC Advances*, 2012, **2**, 9824.

27. S. Zhang, F. Ren, W. Wu, J. Zhou, X. Xiao, L. Sun, Y. Liu, and C. Jiang, *Phys. Chem. Chem. Phys.*, 2013, **15**, 8228.

28. M. Wang, L. Sun, J. Cai, P. Huang, W. Su, and C. Lin, *J. Mater. Chem. A*, 2013, **1**, 12082.

29. Z. G. Jia, D. P. Ren, Y. C. Liang and R. S. Zhu, *Mater. Lett.*, 2011, **65**, 3116.

30. H. Dong, X. L. Li, Q. Peng, X. Wang, J. P. Chen, and Y. D. Li, *Angew.Chem., Int. Ed.*, 2005, **44**, 2782.

31. M. Wang, Z. H. Ai and L. Z. Zhang, *J. Phys. Chem. C*, 2008, **112**, 13163.

32. L. Su, J. Feng, Z. Zhou, C. Ren, H. Li, and X. Chen, *Anal. Chem.*, 2012, **84**, 5753.

33. M. H. Habibi, A. H. Habibi, M. Zendehdel and M. Habibi, *Spectrochim. Acta, Part A*, 2013, **110**, 226.

34. A. A. Tahir and K. G. U. Wijayantha, *J. Photochem.Photobiol. A*, 2010, **216**, 119.

35. R. Zhang, J. Huang, J. Zhao, Z. Sun and Y. Wang, *Energy Fuels*, 2007, **21**, 2682.

36. M. Veith, M. Haas, and V. Huch, *Chem. Mater.*, 2005, **17**, 95.

37. C. Nordhei, K. Mathisen, I. Bezverkhyy, and D. Nicholson, *J. Phys. Chem. C*, 2008, **112**, 6531.

38. Z. H. Yuan, and L. D. Zhang, *Mater. Res. Bull.*, 1998, **33**, 1587.

39. M. Sivakumar, T. Takami, H. Ikuta, A. Towata, K. Yasui, T. Tuziuti, T. Kozuka, D. Bhattacharya, and Y. Iida, *J. Phys. Chem. B*, 2006, **110**, 15234.

40. E. K. Nyutu, W. C. Conner, S. M. Auerbach, C. H. Chen, S. L. Suib, *J. Phys. Chem. C*, 2008, **112**, 1407.

41. S. L. Darshane, R. G. Deshmukh, S. S. Suryavanshi, and I. S. Mulla, *J. Am. Ceram. Soc.*, 2008, **91**, 2724.

42. C. Wang, J. Zhu, S. Liang, H. Bi, Q. Han, X. Liu, X. Wang, *J. Mater. Chem. A*, 2014, **2**, 18635.

43. S. Jana, and A. Mondal, *ACS Appl. Mater. Interfaces*, 2014, **6**, 15832.

44. D. Hu, B. Han, S. Deng, Z. Feng, Y. Wang, J. Popovic, M. Nuskol, Y. Wang, and I. Djerdj, *J. Phys. Chem. C*, 2014, **118**, 9832.

45. S. Mathur, S. Barth, H. Shen, J. C. Pyun, U. Werner, *Small*, 2005, **1**, 713.

46. J. Pan, R. Ganesan, H. Shen, and S. Mathur, *J. Phys. Chem. C*, 2010, **114**, 8245.

47. F. H. Ramirez, J. D. Prades, A. Tarancon, S. Barth, O. Casals, R. J. Diaz, E. Pellicer, J. Rodriguez, J. R. Morante, M. A. Juli, S. Mathur, and A. R. Rodriguez, *Adv. Funct. Mater.*, 2008, **18**, 2990.

48. L. S. Xiao, H. Shen, V. R. Hagen, J. Pan, L. Belkoura, and S. Mathur, *Chem. Commun.*, 2010, **46**, 6509.

49. M. Ahn, K. Park, J. Heo, J. Park, D. Kim, K. Choi, J. Lee, and S. Hong, *Appl. Phys. Lett.*, 2008, **93**, 263103.

50. X. Wang, Y. Wang, D. Åberg, P. Erhart, N. Misra, A. Noy, A. Hamza, J. Yang, *Adv. Mater.*, 2011, **23**, 117.

51. L. Wang, Y. Kang, X. Liu, S. Zhang, W. Huang and S. Wang, *Sens. Actuators, B*, 2012, **162**, 237.

52. T. Sathitwitayakul, M. V. Kuznetsov, I. V. Parkin, R. Binions, *Mater. Lett.*, 2012, **75**, 36.

53. H. Lv, L. Ma, P. Zeng, D. Ke and T. Peng, *J. Mater. Chem.*, 2010, **20**, 3665.

54. Rodriguez-Carvajal J 2001 Commission on powder diffraction (IUCr) Newsletter 26, 12.

55. P. M. P. Swamy, S. Basavaraja, A. Lagashetty, N. V. S. Rao, R. Nijagunappa, and A. Venkataraman, *Bull. Mater. Sci.*, 2011, **34,** 1325.

56. J. Wan, X. Jiang, H. Li and K. Chen, *J. Mater. Chem.*, 2012, **22**, 13500.

57. J. Zhang, J. Shi, M. Gong, *J. Solid State Chem.*, 2009, **182**, 2135.

58. J. Pal, A. K. Sasmal, M. Ganguly, T. Pal, *J. Phys. Chem. C*, 2015, **119**, 3780.

59. W. Cai, J. Yu, S, Gu and M. Jaroniec, *Cryst. Growth Des.*, *2010*, **10**, 3977–3982.

60. M. Zhao, J. Huang, Y. Zhou, X. Pan, H. He, Z. Ye and X. Pan, *Chem. Commun.*, 2013,**49**, 7656.

61. Y. Miyake, H. Togashi, M. Tashiro, H. Yamaguchi, S. Oda, M. Kudo, Y. Tanaka, Y. Kondo, R. Sawa, T. Fujimoto, T. Machinami, and A. Ono, *J. Am. Chem. Soc.*, 2006, **128**, 2172.

62. Y. Tanaka, S. Oda, H. Yamaguchi, Y. Kondo, C. Kojima, and A. Ono, *J. Am. Chem. Soc.*, 2007, **129**, 244.

63. Zhoua, X.; J. Liua, C. Wanga, P. Suna, X. Hua, X. Li, K. Shimanoeb, N. Yamazoeb, and G. Lua, *Sensors and Actuators B*, 2015, **206**, 577.

64. G.Y. Zhang, C.S. Li, F.Y. Cheng, and J. Chen, *Sensors and Actuators B*, 2007, **120**, 403.

65. A. Sutka, G. Mezinskis, A. Lusis, and D. Jakovlevs, *Sensors and Actuators B*, 2012, **171–172**, 204.

66. X.S. Niu, W.P. Du, and W.M. Du, *Sensors and Actuators B*, 2004, **99**, 405.

67. Z. Gergintschew, H. Förster, J. Kostiza, and D. Schipanski, *Sensors and Actuators B*, 1995, **26**, 170.

Hierarchical Growth of $ZnFe_2O_4$ for Sensing Applications

Ramkrishna Sahoo[†], Sumita Santra[‡], Chaiti Ray[†], Anjali Pal[§], Yuichi Negishi[‖], Samit Kumar Ray[‡] and Tarasankar Pal*[,†]

[†]Department of Chemistry, and [§]Department of Civil Engineering, Indian Institute of Technology, Kharagpur-721302, India

[‖]Department of Applied Chemistry, Tokyo University of Science, Tokyo-1628601, Japan

[‡] Department of Physics, Indian Institute of Technology, Kharagpur-721302, India

E-mail: *tpal@chem.iitkgp.ernet.in*

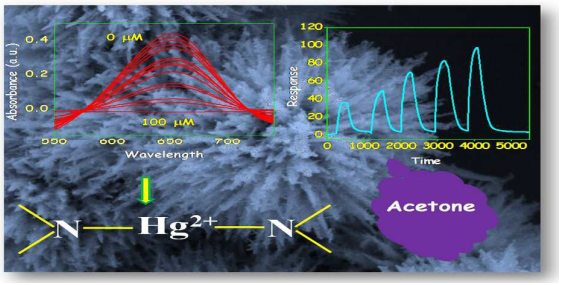

Selective Sensing of toxic heavy metal Hg(II) and environmentally hazardous acetone vapour using mesoporous $ZnFe_2O_4$ NFs, synthesized from our laboratory developed modified hydrothermal technique.